RESEARCH ARTICLE

Product formation during discharge: a combined modelling and experimental study for Li–O$_2$ cathodes in LiTFSI/DMSO and LiTFSI/TEGDME electrolytes

Michael T. Rauter[1,2] · Matthias Augustin[1] · Lena Spitthoff[1,3] · Ann Mari Svensson[1] 🆔

Abstract

Li–air or Li–O$_2$ batteries are a promising energy storage technology due to the potentially high energy density. However, significant challenges related to reversible charge/discharge of these cells need to be solved. The discharge reaction is generally agreed to proceed via two main routes, which may occur simultaneously. These are the surface mechanism, leading to Li$_2$O$_2$ product formation as surface films, or the solution mechanism, with solid particles formed in the pore structure of the cathode. A detailed understanding of the reaction mechanisms and the dynamic performance of the electrodes is key to further improvements. Here, we present a mathematical model for the discharge process, based on porous electrode theory, including effects of reactant transport and kinetic limitations, as well as the continuous change of properties due to the formation of reaction products via the solution mechanism and the surface mechanism. The model describes the dynamic change in the ratio of the surface and solution mechanism as a function of growth of film thickness, in line with recent findings. The model is able to predict the differences in experimentally obtained discharge curves between dimethyl sulfoxide and tetra ethylene glycol dimethyl ether solvents with 1M LiTFSI, with a minimum of free parameters. The model parameters are based on physical characterization of the materials and the electrodes, or determined by fitting to impedance spectra recorded during the discharge. The developed model and the methodology will provide a powerful tool for optimization of such electrodes.

Graphic abstract
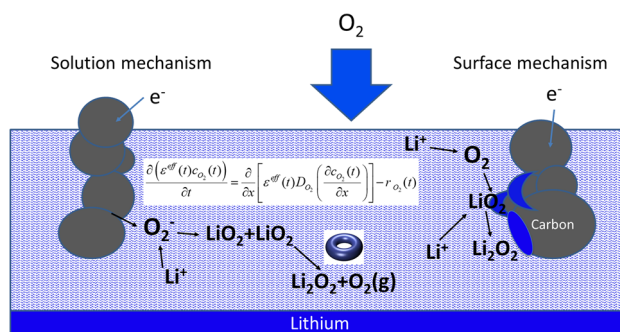
1 Introduction

A battery system which has attracted much attention as a possible alternative for energy storage is the lithium–air (Li–air) battery. Due to their high specific energy [1] it is believed that a fully developed Li–air (or in lab-scale Li–O$_2$) battery system

✉ Michael T. Rauter
   michael.t.rauter@ntnu.no

Extended author information available on the last page of the article

can become a serious competitor to fossil fuels in the transportation sector. However, present Li–air batteries still suffer from a poor cycling stability as well as practical specific energies significantly below the theoretical one. One of the main challenges for a successful development of a practical Li–air battery is the search for an electrolyte that is stable in the reactive environment of the cathode with simultaneous support of the electrochemical reactions. Over the last years, good progress has been made in the understanding of the discharge reaction mechanism of these batteries, and the role of the electrolyte; see i.e. Ref. [2]—for a comprehensive review.

Aprotic electrolytes have dominated the Li–air battery development over the past ten years. The reasons for this are the low ionic conductivity of the solid-state electrolyte and the instability of lithium metal against aqueous electrolytes which often causes corrosion and H_2 formation [3, 4]. The desired reaction product at the cathode is the lithium peroxide, Li_2O_2, and the overall reaction in the cathode is given as

$$2Li^+ + O_2 + 2e^- \leftrightarrow Li_2O_2 \tag{1}$$

It is known that the formation of the discharge product (Li_2O_2) leads to passivation of the active surface and blockage of the pores [5]. Therefore, the formation and deposition morphology of Li_2O_2 have been the focus of recent research activities [6, 7]. It has been experimentally verified, that the deposition morphology of Li_2O_2 is strongly dependent on the electrolyte properties [5] and the discharge current [8]. Li_2O_2 is formed via two main reaction pathways: the surface-based mechanism forming a film on the electrode surface and the solution-based mechanism forming crystalline toroids in the electrolyte, which are attached to the electrode surface [9].

For both the solution and solvation pathway, the formation of Li_2O_2 follows a multi-step reaction [6]. First, oxygen is reduced by one electron.

$$O_2 + e^- \rightarrow O_2^- \tag{2}$$

The further reaction can either happen on the surface or in the solution. Following the proposed reaction mechanism of Xue et al. [10] it is believed that for the surface mechanism the reduced oxygen reacts with Li^+ to form LiO_2 as an intermediate product. Subsequently, LiO_2 reacts with one more electron and Li^+ to form the end product Li_2O_2 as a film which is covering the electrode surface.

$$O_2^- + Li^+ \rightarrow LiO_2 \tag{3}$$

$$LiO_2 + Li^+ + e^- \rightarrow Li_2O_2 \tag{4}$$

For the solution-based mechanism it is assumed that the reduced oxygen is transported through the electrolyte to a preferred nucleation site to form toroids [10].

$$2O_2^- + 2Li^+ \rightarrow Li_2O_2 + O_2 \tag{5}$$

Alternatively, expressed as subsequent chemical disproportionation as competing reaction, see Laoire et al. [11].

$$LiO_2 + LiO_2 \rightarrow Li_2O_2 + O_2 \tag{6}$$

It is generally agreed that the dominating mechanisms is determined by the basicity of the solvent, as given by the Gutman donor number (DN) [2], as well as the discharge current density [2]. Typical examples of solvents used for Li–air batteries are TEGDME and DMSO, representing low and high Lewis basicity solvents with DNs of 16.6 and 29.8, respectively [10, 12]. The basicity reflects the ability of the solvent to solvate O_2^-/LiO_2, a governing factor with respect to the dominating mechanism. When high DN electrolytes are used, the solvated LiO_2 intermediates subsequently disproportionate to solid, crystalline, toroidally shaped Li_2O_2 particles [13–15]. With low DN solvents and/or high current densities and overpotentials, the discharge reaction proceeds via the surface growth pathway. For the surface pathway, the discharge capacity is typically limited by the film resistance, which will increase dramatically when the film thickness grows beyond 5–10 nm [2, 16, 17]. For the solution pathway, the product formation also causes a gradually increasing overpotential and local current density, which again leads to a shift in the reaction mechanism towards the surface pathway, and eventually passivation due to blocking of the active surface. A detailed study of the product formation during charge and discharge (at various states of charge) has been undertaken by Augustin et al. [7], using both SEM surface and cross-sectional analysis.

Mathematical models for the electrochemical performance of porous cathodes for Li–air batteries are usually developed within the framework of the porous electrode theory [18]. A review of modelling work is provided in Ref. [19]. Models have been developed describing either the surface mechanism, see e.g [20], or with a focus on optimization of the pore network [21, 22]. In Ref. [22], a continuum model was developed, where the oxygen reduction reaction (ORR) was modelled as a multistep reaction using different rate constants. The rate of solution vs. surface mechanism was controlled simply by the choice of the kinetic parameters. The model was validated based on experimental results. Xue et al. [10] presented an alternative description of the two pathways for the ORR in their model by introducing a so called escape probability as measure of the ratio between the two pathways. The escape probability was a function of the pore diameters and volumes. However, the escape probability was treated as constant and did not take into account the dynamic change of the porosity during discharge.

In this work, we have developed a continuum type model for the Li–air cathode, in order to describe the discharge

reaction, incorporating both mechanisms (i.e. the surface and the solution pathway) as simultaneously occurring processes in the electrode. The transport of dissolved oxygen, the kinetics of the ORR, as well as ohmic losses are included in the model. An escape parameter was introduced, taken to be a function of the resulting film thickness, in line with recent findings in the field. This allowed for a dynamic description of the discharge process. The discharge model was coupled to an impedance model to account for the dynamic change of the impedance response during discharge. Model parameters could be determined in a robust manner by combining data from electrochemical impedance spectroscopy and galvanostatic discharge. A good agreement with experimentally obtained discharge curves for LiTFSI/DMSO and LiTFSI/TEGDME electrolytes could be achieved with a minimum of free parameters.

2 Experimental

The cathode was manufactured by casting a paste, consisting of Vulcan® XC72 carbon black (from Cabot Corp.) and a binder-solution (Polyvinylidene difluoride, PVDF, ≥ 99%, from AME Energy Co., Ltd.), onto carbon paper (PTFE treated TGP-H-60 Toray from Alfa Aesar). For the binder solution 0.6 g of PVDF was mixed with 6 g N-methyl-2-pyrrolidine (NMP, anhydrous, 99.5% from Sigma Aldrich) and stirred for 45 min. NMP was added 3 times each time followed by 25 min shaking in ball milling jars in order to obtain a homogeneous paste. The total carbon:PVDF ratio was 9:1. The paste was applied with a wet casting thickness of 120 μm onto the carbon paper. The wet electrode cast was pre-dried at 60 °C for 45 min and subsequently heated overnight at 85 °C under vacuum in order to remove residual NMP. The dry cast was transferred to a glovebox with argon atmosphere, where discs with diameters of 16 mm were cut from the cast. The gas diffusion electrodes (GDE) were weighed and stored in argon atmosphere until used. The carbon black loading of the electrodes was 3.28 mg ± 0.15 mg. The two electrolyte solvents used were tetraethylene glycol dimethyl ether (TEGDME, 99%, from and Acros Organics), and dimethyl sulfoxide (DMSO, anhydrous, ≥ 99.9%, from Sigma Aldrich), which were mixed with lithium bis(trifluoromethanesulfonyl)imide (LiTFSI, 99.95% trace metals basis, from Sigma Aldrich). Electrolytes were prepared in a glove box (MBRAUN) in an Ar atmosphere with < 0.1 ppm H_2O and < 0.1 ppm O_2. A molar concentration of 1M LiTFSI in DMSO and TEGDME was used. All chemicals were used as purchased without further purification. The assembly of the test cells was carried out in a glovebox system with argon atmosphere, using the ECC-Air setup from EL-CELL® GmbH

The measurements were carried out at ambient temperature with a VMP-300 multipotentiostat (Bio-Logic Science Instruments). The cells were constantly supplied with an oxygen flow of 4 mL/min (gas purity: 5.0, AGA AS). The cells were discharged and charged with a current density of i = 75 mA/g_C, where g_C is the mass of Vulcan® XC72 carbon black. The potential range was ΔE = 2.4–4.15 V vs. Li/Li$^+$. Before the first discharge the battery system was oxygenated for two hours at open-circuit voltage (OCV).

Impedance measurements were performed during the first discharge at regular intervals, in the frequency range between 20 kHz and 2 mHz. At every point impedance was recorded with 5 measurement points per frequency decade. All impedance measurements were done with the use of a Li metal reference electrode. The capacity of the cells was calculated based on the mass of the carbon (Vulcan® XC72). This was done in order to account for the reaction surface area which scales proportionally to the carbon mass, and is common practice for Li–O_2 porous cathodes [2, 23–25].

3 Model development

3.1 Discharge model

The active layer of the cathode is treated as a network of ideal spherical particles with a diameter of 50 *nm* to account for the spherical shape and the size of the *Vulcan*® XC72 carbon black particles. In the model the active layer with a measured total thickness of 35 μm is treated as one dimensional and divided into n = 20 segments. The change of the system due to product formation, is updated with a time step size of dt = 10 s. Concentration variations of Li$^+$ in the active layer are neglected, as the Li$^+$ transport is assumed to not be a limiting factor. This assumption is made on the basis of the high mobility of Li$^+$ in the chosen electrolytes [12], and the much higher Li$^+$ concentration compared to the oxygen concentration. Also, Li depletion is avoided, as the anode is metallic lithium.

The mass conservation equation for oxygen (i.e. non-charged species in a stagnant electrolyte without convection), can be written as:

$$\frac{\partial(\varepsilon_j^{\text{eff}} c_{O_2,j})}{\partial t} = \frac{\partial}{\partial x}\left[\varepsilon_j^{\text{eff}} D_{O_2}\left(\frac{\partial c_{O_2,j}}{\partial x}\right)\right] - \frac{i_{\text{vol},j}}{\nu F} \tag{7}$$

where $c_{O_2,j}$ is the concentration of oxygen, $\varepsilon_j^{\text{eff}}$ is the effective porosity and $i_{\text{vol},j}$ the volumetric discharge current in each segment j. D_{O_2} is the diffusion coefficient of oxygen in the electrolyte, $\nu = 2$ is the number of electrons involved in the overall reaction and F is the Faraday constant. Equation 7 was solved with the following boundary conditions

$$t = 0, \text{all x}, c_{O_2,j} = c_{O_2}^{\text{sat}}$$
$$x = 0, \text{all t}, c_{O_2,j} = c_{O_2}^{\text{sat}}$$
$$x = L = 35\mu m, \text{all t}, \frac{\partial c_{O_2,j}}{\partial x} = 0$$

The tortuosity of a bed of spherical particles is described by the well known Bruggeman correlation for spherical particles.

$$\varepsilon_j^{\text{eff}}(t) = b_j(t)^{1.5} \varepsilon_0^{1.5} \qquad (8)$$

where b_j is a factor that describes the blockage of pores as a function of the initial porosity, ε_0, and the volume fraction $\varepsilon_{\text{prod},j}$ of the discharge product in each segment

$$b_j(t) = \frac{\varepsilon_0 - \varepsilon_{\text{prod},j}}{\varepsilon_0} \qquad (9)$$

Following Faraday's law, the total amount of the formed product (Li_2O_2) for each segment can be described by integrating the total current I_j in each segment over time:

$$n_j(t) = \frac{1}{\nu F} \int_0^t I_j \mathrm{d}t \qquad (10)$$

Here, the total current I_j in each segment is directly related to the volumetric discharge current $i_{\text{vol},j}$ in Eq. 7 by

$$i_{\text{vol},j} = \frac{I_j}{V_j} \qquad (11)$$

where V_j is the volume of each segment. The total current I_j in each segment is calculated using the Butler–Volmer equation as described later. The total amount of formed product $n_j(t)$ is then used to calculate the volume fraction of the product at a specific time t in each segment.

Due to the two different pathways for product formation, Xue et al. [10] proposed a model that is considering both, the Li_2O_2 growth as a film on the surface of the cathode and the growth as toroids in the electrolyte. The group introduced an escape function based on the pore size distribution in order to determine the proportion of product which contributes to the film formation. The idea of an escape function is adopted in this work, but instead of a simple dependence on the initial pore size distribution, the escape probability is described as a function of film thickness. It is assumed that the probability, χ_{escape}, of product being formed in the electrolyte decreases with an increase of film thickness and corresponding increase of the resistance. This assumption is supported by a work of Adams et al. [8] who stated that LiO_2 has a stronger adsorption to the Li_2O_2 film than to the carbon surface. Thus, it is possible that an increase of film thickness leads to a stronger adsorption towards LiO_2 and therefore decreases the probability of the solution-based mechanism to occur. The following escape function was introduced:

$$\chi_{\text{escape}}(t) = \zeta_{\text{sol}} \left[\frac{1 - erf(\frac{\delta(t) - \delta_{\text{crit}}}{10})}{2} \right] \qquad (12)$$

ζ_{sol} was fitted to the discharge curve and corresponds to the percentage of product which is formed by the solution-based mechanism at the beginning of the discharge. The decrease of the escape probability with a larger film thickness is described by the use of an error function, where δ is the film thickness averaged over all segments and δ_{crit} is the critical film thickness. In accordance with Viswanathan et al. [26] the critical film thickness was set to $\delta_{\text{crit}} = 5$ nm. The steepness of the error function was adjusted by division with a factor of 10.

The escape probability is used to calculate the volume fraction of the product resulting from the film formation on the active surface of the cathode, and the following equation is assumed:

$$\varepsilon_{\text{film},j}(t) = \varepsilon_{\text{prod},j}(t)(1 - \chi_{\text{escape}}(t)) \qquad (13)$$

For the calculation of the film thickness, the film is assumed to grow homogeneously on the surface of the spherical carbon particles. With the given assumptions the film thickness δ can be derived from the volume fraction of the particle $\varepsilon_{\text{part}}$ and the discharge product $\varepsilon_{\text{film}}$ that is formed by the surface mechanism:

$$\delta(t) = \left[\sqrt[3]{\frac{\varepsilon_{\text{part}} + \varepsilon_{\text{film}}(t)}{\varepsilon_{\text{part}}}} - 1 \right] r_{\text{part}} \qquad (14)$$

During discharge, an increasing amount of Li_2O_2 deposits on the surface of the carbon particles, thus causing a decrease of the active surface area and hindering the supply with Li^+ and O_2. Consequently, the reduction of the carbon surface by coverage of Li_2O_2 plays a key role in the discharge behavior of the battery.

Following the empirical equation of Sahapatsombut et al. [27], the reduction of active surface area is calculated by:

$$A_j(t) = A_{0,j} \left[1 - \left(\frac{\varepsilon_{\text{film},j}(t)}{\varepsilon_0} \right)^p \right] \qquad (15)$$

where $A_{0,j}$ is the surface area. Exponent p is a geometrical factor that describes the morphology of Li_2O_2 covering the active surface area. In accordance with the literature, where values between 0.4 and 0.5 are used [27, 28], p was fixed to a value of 0.45.

The passivation of the surface area during discharge is known to be caused by the insulating Li_2O_2 film, which inhibits the charge transfer to the Li_2O_2—electrolyte interface, where the electrochemical reactions occur and thus causing an ohmic voltage loss [5, 29]. Similar to other approaches in the

literature [30–33], the film resistance is described in this work by a linear dependence of the film thickness δ. However, when the film approaches a critical film thickness δ_{crit}, representing the critical thickness for electron tunnelling [29], electrochemical reactions are kinetically hindered, and we expect a strong increase of the resistance. This strong resistance increase is accounted for by the use of the error function with the same critical film thickness $\delta_{crit} = 5$ nm as in Eq. 12:

$$R_{film,dis} = \frac{\varrho_s \delta}{\frac{1 - erf\,(\delta - \delta_{crit})}{2}} \tag{16}$$

where ϱ_s is the resistivity and is used as a fitting parameter within the range of the literature values [30–32]. Note that the unit of $R_{film,dis}$ is [Ωm^2].

It is assumed that the faradaic current can be described by a Butler–Volmer equation. Following the proposed equation of Bard et al. [34] the Butler–Volmer equation can be expressed as:

$$i_{far} = vFkc_{O_2}\left[\exp\left(\frac{\beta F\eta}{RT}\right) - \exp\left(-\frac{(1-\beta)F\eta}{RT}\right)\right] \tag{17}$$

where k is the kinetic rate, β the charge transfer coefficient and η the activation overpotential. The oxygen reduction rate k is fitted to the first impedance measurement. The Butler–Volmer overpotential is treated as homogeneous across the active layer. For simplification a value of 0.5 was chosen for β.

With the given assumptions it is possible to express η as a function of the applied discharge current density i_a and the averaged oxygen concentration of all segments c_{O_2}:

$$\eta = \frac{2RT}{F}\sinh^{-1}\left(\frac{i_a}{2vFkc_{O_2}}\right) \tag{18}$$

with

$$i_a = \frac{I}{A_{ac}} \tag{19}$$

where I is the overall total discharge current and A_{ac} the total active surface area. The overall cell voltage can be calculated by the following equation:

$$U = U_0 - \eta - i_a R_{film,dis} - i_{a,cell} R_s \tag{20}$$

where R_s is the series resistance, $i_{a,cell}$ the discharge current regarding the cross sectional cell area and $R_{film,dis}$ the film resistance. Thus, i_a is the discharge current density with respect to the active surface of the carbon, while $i_{a,cell}$ is the discharge current density with respect to the cross section of the battery cell.

The parameters used in the discharge model are given in Table 1.

Table 1 Parameters used in the model

Parameter	Symbol	Value	Unit	Source
Particle size	r_0	50	[nm]	Manufacturer's specification
Initial porosity	ε_0	0.78	[–]	Calculated
Volume fraction of the particles	ε_c	0.22	[–]	Calculated
Temperature	T	298.15	[K]	Measured
Faraday constant	F	96,485	[C/mol]	–
Gas constant	R	8.315	[kg m^2/s^2 mol K]	–
Molecular weight Li$_2$O$_2$	$M_{Li_2O_2}$	45.88	[g/mol]	[35]
Density Li$_2$O$_2$	$\rho_{Li_2O_2}$	2310	[kg/m^3]	[35]
Gross cell area	A_{gross}	2.01	[cm^2]	Measured
Specific carbon surface area	a_0	237	[m^2/g]	[36]
Cathode thickness	L_{cat}	35	[µm]	Measured
TEGDME				
O$_2$ diffusion coefficient	D_{O_2}	$2.17e^{-10}$	[m^2/s]	[12]
Saturated O$_2$ concentration	$c_{O_2}^{sat}$	4.43	[mol/m^3]	[12]
DMSO				
O$_2$ diffusion coefficient	D_{O_2}	$1.67e^{-9}$	[m^2/s]	[12]
Saturated O$_2$ concentration	$c_{O_2}^{sat}$	2.10	[mol/m^3]	[12]

4 Impedance model

The elements for the equivalent circuit model were chosen analogous to Eq. 20 of the discharge model. Accordingly, the contributions to the total impedance consist of a series resistance (R_s), a charge transfer resistance (R_{ct}) and the resistance caused by the film ($R_{film,imp}$). To account for the capacitance of the electrode and the film, R_{ct} and $R_{film,imp}$ were connected in parallel to constant phase elements. In electrochemical systems, the impedance response of the charge transfer resistance often follows a distributed reactivity which is generally represented as a constant phase element (CPE) [37]. As a reference electrode was used (lithium), the equivalent circuit models are representing the mechanisms within the cathode. Using the same approach for the description of the film resistance in combination with the series resistance, the overall expression of the equivalent circuit is:

$$Z(\omega) = R_s + \frac{R_{ct}}{1 + (j\omega)^{\alpha_{ct}} Q_{ct} R_{ct}} + \frac{R_{film,imp}}{1 + (j\omega)^{\alpha_{film}} Q_{film} R_{film,imp}} \tag{21}$$

The equation for the charge transfer resistance can be directly derived from Eq. 17 of the discharge model:

$$R_{ct} = \left(\frac{\partial \eta}{\partial i_{far}}\right)_{\eta_{meas}} = \frac{RT}{\nu F^2 k c_{O_2} \sqrt{\frac{i_{far}^2}{(2\nu F k c_{O_2})^2 + 1}}} \tag{22}$$

The oxygen reduction rate k was determined from the value of R_{ct} obtained by fitting to the first impedance measurement. This value of the oxygen reduction rate was used in Eq. 18 of the discharge model. Thus, the charge transfer resistance, R_{ct}, is changing with discharge time, depending on the oxygen concentration c_{O_2} and the faradaic current i_{far} (both computed by the discharge model). The capacitance of the electrode, Q_{ct} was calculated to be 35 F/g in relation to the mass of the carbon black. Also the contribution of the film to the total impedance is changing with discharge time and is calculated by division of the total film resistance (as computed in Eq. 16) with the surface of the film.

$$R_{film,imp} = \frac{R_{film,dis}}{A_{film}} \tag{23}$$

where the film surface is calculated by:

$$A_{film} = 4\pi(r_{part} + \delta_s)^2 \tag{24}$$

where r_{part} is the radius of the carbon black particle and δ_s is the film thickness as calculated in Eq. 14 in the discharge model.

A value of 50 μF/cm² is used for the calculation of the double layer capacitance of the Li_2O_2-electrolyte interface, Q_{film}, which is typically in the range of 10–50 μF/cm² as given by Huang et al. [38]. As A_{film} is increasing with time the capacitance of the film is increasing accordingly.

To account for heterogeneity's or non-uniform current distributions, α_{ct} and α_{film} were used as fitting parameters, with reasonable values in the range of 1 to 0.7 [39].

The coupling between the discharge and the impedance model of the first discharge is based on the direct relation between Eqs. 18 and 22 as well as Eqs. 16 and 23. The time-dependent parameters needed for the simulation of the impedance spectra are calculated from the discharge model.

5 Results and discussion

The discharge performance was simulated based on the parameters given in Table 1, providing the parameters determined from the experimental discharge curves and impedance spectra as shown in Table 2.

The simulated discharge curves are compared to experimental data in Fig. 1 for (a) LiTFSI/DMSO and (b) LiTFSI/TEGDME. The points at which impedance measurements were made during discharge are marked with crosses and the simulated time of reaching the critical film thickness with δ_{crit}. The capacity of the cells was calculated based on the mass of the carbon (Vulcan® XC72). A discussion on true electrode capacities for porous electrodes is given in [2].

A comparison of the first discharge of LiTFSI/DMSO and LiTFSI/TEGDME in Fig. 1 shows better initial electrochemical properties of the DMSO-based electrolyte than the one based on TEGDME. Three advantages of the system with LiTFSI/DMSO are particularly striking: The higher discharge capacity, the potential at which the discharge takes place and the oxygen reduction rate k, which was found to

Table 2 Parameters obtained by fitting of the coupled discharge-impedance model to experimental data for LiTFSI/DMSO and LiTFSI/TEGDME

Parameter	Symbol	LiTFSI/DMSO	LiTFSI/TEGDME	Unit
Oxygen reduction rate	k	6.1e−10	2.5e−10	[m/s]
Escape parameter	ζ_{sol}	0.87	0.25	[–]
Li_2O_2 film resistivity	ϱ_{film}	9e8	4e9	[Ωm]
Form parameter (electrode)	α_{ct}	0.95	0.95	[–]
Form parameter (film)	α_{film}	0.95	0.95	[–]

Fig. 1 Comparison between experimental and simulated data of the voltage-capacity curve for a LiO$_2$ battery with **a** LiTFSI/DMSO and **b** LiTFSI/TEG-DME as electrolyte. The points for impedance measurements during discharge are marked with circles and the simulated time of reaching the critical film thickness with δ_{crit}. The cells were discharged with a current density of i = 75 mA/g_C within a potential range of ΔE = 2.4–4.15 V vs. Li/Li$^+$
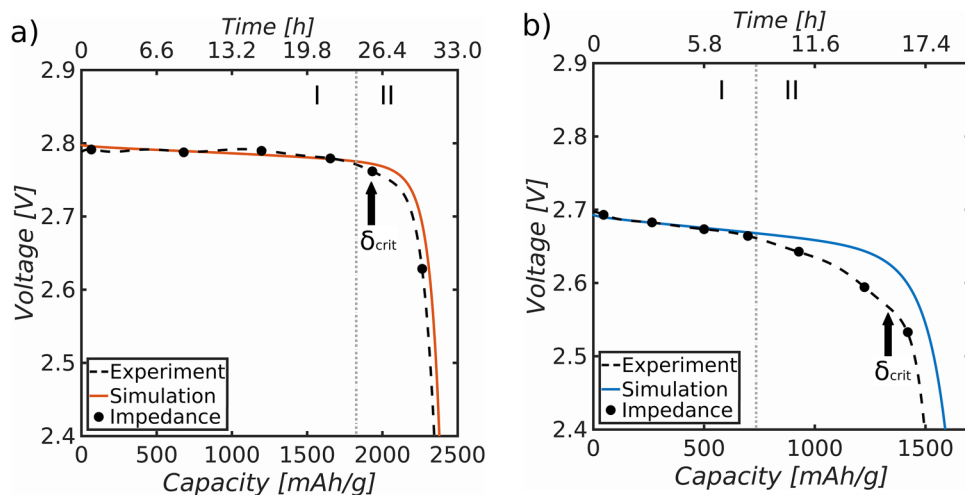

Fig. 2 Experimental Impedance measurements performed during the first discharge as marked in Fig. 1 for LiTFSI/TEGDME and LiTFSI/DMSO. The impedance illustration are divided in two sections (I and II) corresponding to the discharge curves. The graphs are **a** section I of LiTFSI/DMSO **b** section I of LiTFSI/TEGDME **c** section II of LiTFSI/DMSO and **d** section II of LiTFSI/TEGDME
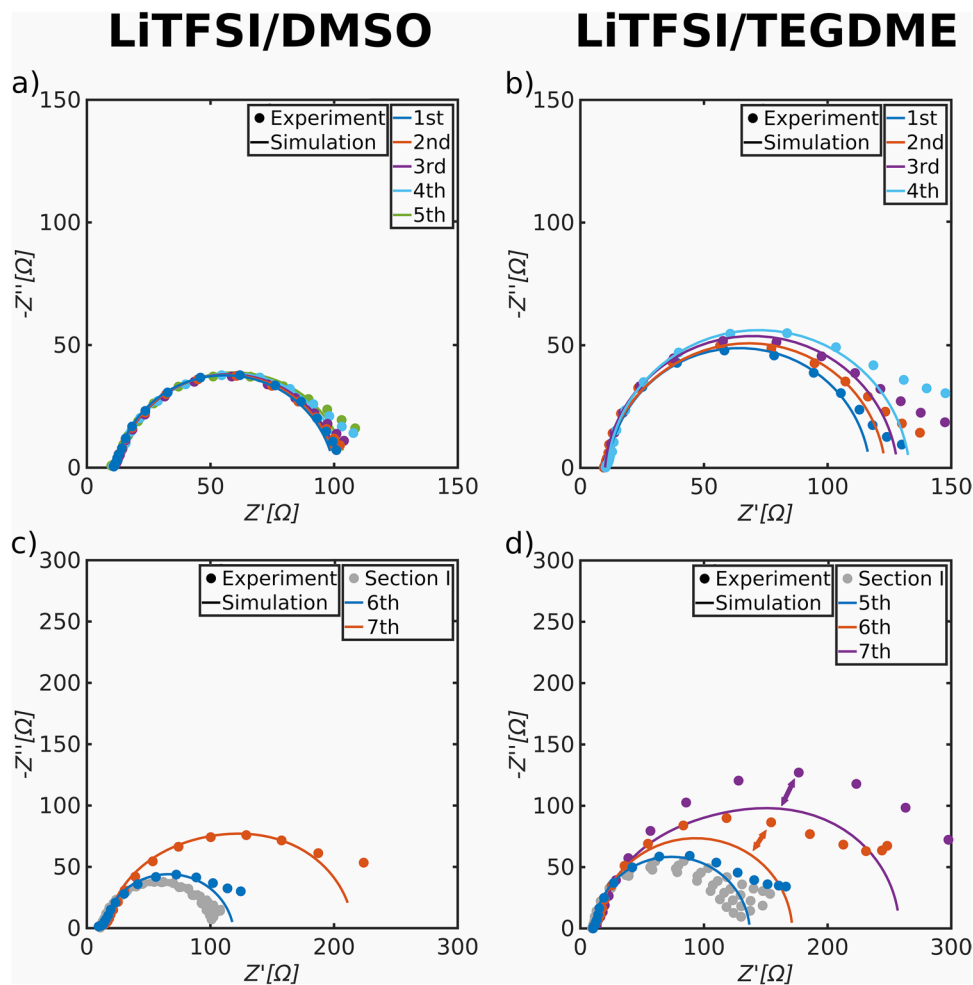
be almost 2.5 times higher in LiTFSI/DMSO than in LiTFSI/TEGDME (see Table 2).

The impedance spectra recorded during the first discharge are shown in Fig. 2. Good agreements are obtained by fitting of the simple model to both the discharge curve and the impedance spectra with a minimum of free

parameters (see Table 2). Thus, incorporating passivation of electrodes by the growth of the surface film, with a critical thickness corresponding to 5 nm, provides realistic model description.

The first impedance measurements in Fig. 2 of (a) LiTFSI/DMSO shows a smaller semi-circle in the system

compared to the one in (b) LiTFSI/TEGDME. Since the first impedance measurement was made in the very beginning with a negligible amount of product, the size of the semi-circle is dominated by the charge transfer resistance R_{ct}. The difference between the impedance spectra of the DMSO and TEGDME electrolytes reflects the higher oxygen reduction rate k in LiTFSI/DMSO (compare Eq. 22). This is particularly remarkable since the oxygen concentration is lower in LiTFSI/DMSO than in LiTFSI/TEGDME (see Fig. 3b) which has a negative impact on the charge transfer resistance. Laoire et al. [12] were able to show a dependence of the oxygen reduction rate on the Gutmann donor number (DN) of the solvent. Here, the oxygen reduction rate was higher in solvents with a high DN compared to the ones with a lower one. This finding of Laoire et al. is in good agreement with the oxygen reduction rates obtained in this work and is furthermore supported by a more recent work of Amin et al. [40] who also showed the influence of solvents on the reaction kinetics. The results here confirm the previous findings that a high DN does not only result in a higher discharge capacity but also increases the oxygen reduction rate resulting in a lower charge transfer resistance and a higher discharge voltage.

Section II of the discharge curve of LiTFSI/TEGDME shows a stronger voltage decrease and a double plateau formation, which is not in agreement with the curve predicted by the model. Similarly, when comparing the experimental impedance measurements to the simulated ones (see Fig. 2d), the model cannot account for the increase in resistance as observed in section II. The fact that the discharge curve exhibit two plateaus, as demonstrated also by the presence of two peaks in the differential capacity plots of Augustin et al. [7], indicates that a second electrochemical process occurs. In accordance with Ref. [7], the most likely explanation is the Li_2O_2 formation via the surface growth pathways (Eqs. 3–5), known to dominate for the TEGDME solvent. Another process that might lead to this, is the formation of Li_2CO_3 through side-reactions, as shown by Ottakam

et al. [41], who identified side reactions with Li_2CO_3 as main product both for DMSO and TEGDME electrolyte solvents.

DMSO was found to be more stable than TEGDME which results in smaller amounts of Li_2CO_3 in the DMSO-based electrolyte than in the one based on TEGDME. This finding is supported by the work of Augustin et al. [7] who found Li_2CO_3 to be present after the first discharge in both electrolytes (LiTFSI/DMSO and LiTFSI/TEGDME). Albertus et al. [32] compared the bandgaps of Li_2O_2 and Li_2CO_3 and stated that the electronic resistivity of Li_2O_2 is orders of magnitude smaller than the one of Li_2CO_3. This indicates that already a small layer of Li_2CO_3 would significantly increase the resistivity of the film, thus contributing to a voltage decay in the discharge curve and increasing the semi-circle diameters of the impedance measurements.

Figure 3 shows the simulated distribution of (a) product saturation, i.e. the free pore volume filled with product, and (b) oxygen concentration within the active layer at the end of the first discharge. Both, the product saturation and the oxygen concentration are plotted against the location within the active layer for LiTFSI/DMSO and LiTFSI/TEGDME. The oxygen concentration at 35 µm was fixed to the oxygen saturation concentration of the corresponding electrolyte (see Table 1). The product saturation is on a higher level for LiTFSI/DMSO compared to the one of LiTFSI/TEGDME. Both product saturation distributions show a gradual decrease with a higher saturation at the oxygen inlet and a lower one at the side facing the separator. Here, the gradient is significantly larger in the system with LiTFSI/TEGDME than in the one with LiTFSI/DMSO. The gradient of the oxygen concentration in behaves in a similar way with a significantly larger gradient for LiTFSI/TEGDME than for LiTFSI/DMSO. For both electrolytes, with a strong oxygen gradient in LiTFSI/TEGDME and almost constant distribution in LiTFSI/DMSO, there is no oxygen shortage during the first discharge.

The simulated film thickness and the ratio between the two product formation mechanisms are shown in Fig. 4a, b,

Fig. 3 Distribution of **a** product saturation and **b** oxygen concentration across the active layer for LiTFSI/DMSO and LiTFSI/TEGDME. The oxygen inlet is on the right side of the graphs at 35 µm and the separator on the left side at 0 µm
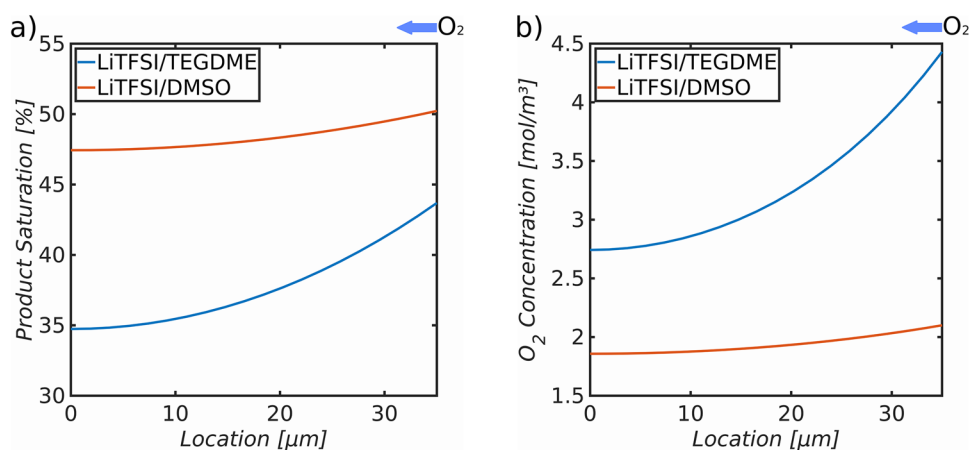
respectively. The main increase of the electrode resistance as observed from the impedance spectra are attributed to an increase in the film resistance. Figure 4b shows that the percentage of the current consumed by the solution-based mechanism in LiTFSI/TEGDME is 19% at the beginning and linearly decreases towards 10%. On the opposite, the dominant mechanism at the beginning of the discharge of the system with LiTFSI/DMSO as electrolyte is, according to the model, Li_2O_2 formation via the solution pathway. However, the ratio between the two mechanisms for LiTFSI/DMSO changes during discharge, as the percentage of 65% for the solution mechanism gradually decreases to 35% from start to end of discharge. The decrease of the escape probability with progressing discharge in the model is caused by the assumed dependency of the film thickness in Eq. 12 and induces a further increase of the film formation rate.

There are several reports in the literature which suggest that electrolyte solvents with a high Gutmann donor number (DN) enhance Li_2O_2 formation via the solution mechanism rather than a formation via the surface pathway [12, 42, 43]. Another explanation of the solution-based mechanism was given by Adams et al. [8] who proposed that the solution pathway is caused by solvation of the intermediate product LiO_2, which is similar to the solvation of O_2^-, dependent on the stabilization within the electrolyte. Disregarding the uncertainty which intermediate product is responsible for the solution mechanism, the product formation takes place via both mechanisms in both electrolytes, as has been reported [2, 7]. In the work of Augustin et al. [7], Li_2O_2 was found as toroids and as film covering the electrode surfaces in both electrolytes, LiTFSI/DMSO and LiTFSI/TEGDME.

In the model, the film thickness is not only influencing the ratio between surface to solution mechanism, but is also responsible for the voltage decrease in the discharge curve of LiTFSI/TEGDME in section I. This finding is based on the good correlation between the discharge curves and the impedance measurements, as a comparison of R_{ct}

and $R_{film,imp}$ showed that it is particularly the resistance of the film which is contributing to the increase of the impedance response. The linear increase of the corresponding impedance measurements can therefore be directly related to an increase of $R_{film,dis}$ (Eqs. 16 and 23) in the model. This is in contrast to the discharge model of Lau et al. [44] who assumed the voltage decrease to be caused by the reduction of the active surface, but corresponds to other studies who proposed the film to be responsible for the voltage decline [26, 45]. Furthermore, the good agreement of the discharge and impedance model in section I for both electrolytes points out that Li_2O_2 is most likely the main discharge product during the first part of discharge for both electrolytes. Here it is notable that the resistivity of the film was found to be higher in LiTFSI/TEGDME than in LiTFSI/DMSO. This is in agreement with the studies of Xue et al. [10] who investigated the dependence of the film resistivity on the discharge current and found the resistivity of the film in an electrolyte with DMSO as solvent to be lower than the one in an electrolyte with TEGDME as solvent. In section II of the discharge the model fits to the experimental discharge and impedance behaviour of LiTFSI/DMSO but shows deviations compared to experimental data of LiTFSI/TEGDME. The gradual decrease of the discharge curve with LiTFSI/DMSO as electrolyte begins when approaching the calculated critical film thickness and shows a sharp voltage drop after reaching it (see Fig. 1a). In contrast, the discharge curve of LiTFSI/TEGDME decreases earlier and independent of the calculated critical film thickness but shows the same sharp voltage drop after reaching it (see Fig. 1b). The calculated film thicknesses at the end of discharge of 6.6 nm for LiTFSI/DMSO and 6.1 nm for LiTFSI/TEGDME are within the range of 5–10 nm reported as the critical film thickness for electron tunneling [26].

The given results of the discharge behavior and the presence of enough oxygen in both electrolytes, indicate that

Fig. 4 Simulated **a** film thickness δ and **b** escape probability χ_{escape} plotted over discharge time for LiTFSI/DMSO and LiTFSI/TEGDME
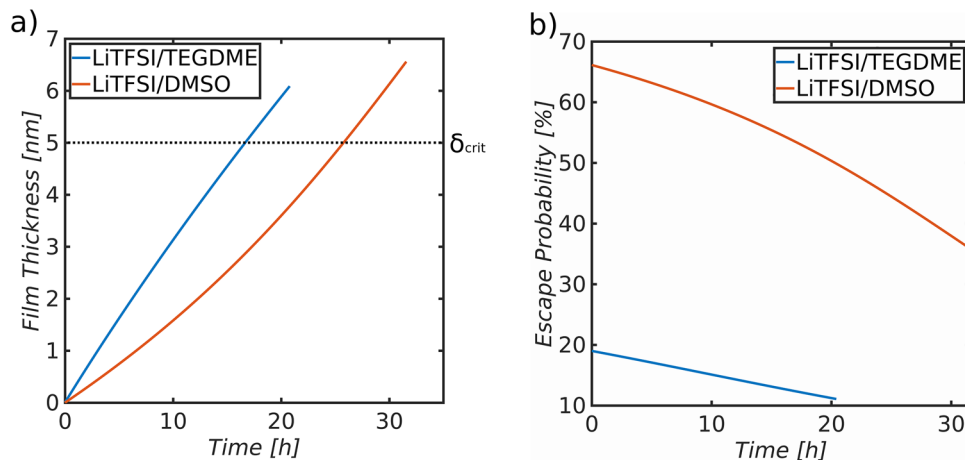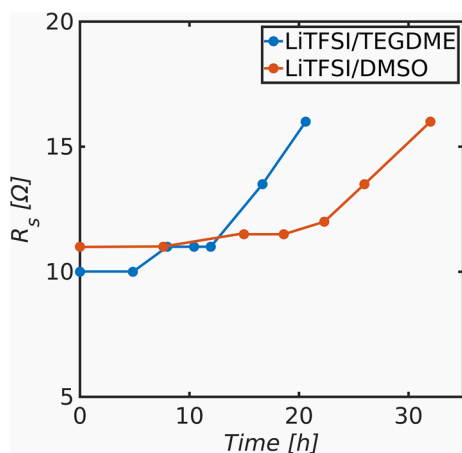
Fig. 5 Series resistance plotted over discharge time for LiTFSI/DMSO and LiTFSI/TEGDME

the main limitation of the first discharge for both electrolytes is the film covering the electrode surface. Since the voltage of both systems drops significantly when reaching the calculated critical film thickness, this suggests electron tunneling through the film which stops when the film is too thick to support electrochemical reactions. This is also in good agreement with the higher capacity (i.e. longer discharge time) of the system with LiTFSI/DMSO as electrolyte, as the growth of the film is slower compared to the one in LiTFSI/TEGDME (see Fig. 4a)). This is assigned here to the enhanced product formation via the solution mechanism in LiTFSI/DMSO.

Besides the analogous behavior of the discharge curve and the impedance measurements, it is also noticeable that the series resistance in Fig. 5 is behaving in accordance to the discharge curve too. Here, the series resistance of the system with LiTFSI/TEGDME is increasing almost from the start, whereas the one of LiTFSI/DMSO remains nearly constant, followed by a gradual increase when approaching the end of discharge. Since the shape of the discharge curve seems to be influenced by the effective thickness of the film, this suggests that the series resistance is also a function of the film thickness. As the series resistance of batteries is dependent on the electrolyte and electrode conductivities as well as the contact resistance [46], three scenarios are possible here. First, the electrolytes are degrading during discharge, which leads to a decay of the electrolyte conductivity. The second and the third scenario are related to the film formation on the surface of the electrodes. It is conceivable that the film growth leads to a contact loss between (a) the carbon particles themselves and (b) the carbon particles and current collector. This loss of contact would result in a decrease of conductivity between the carbon particles and increase of contact resistance between the carbon particles and the current collector. Since significant electrolyte

degradation in electrolytes based on TEGDME was reported to occur only during charge [47, 48], scenario two and three are more likely to influence the serial resistance in both electrolytes during the first discharge.

6 Conclusions

A mathematical model has been developed describing the discharge performance of Li–air batteries, including the transport of dissolved oxygen in the porous carbon electrode, the kinetics of the oxygen reduction reaction, as well as the growth of a surface film and formation of dissolved, solid products inside the pores, by the so-called surface and solution mechanisms, respectively. The model accounts for the recent findings in the field by introduction of an escape parameter describing the ratio of the surface and solution mechanism, as a function of the thickness of the discharge product surface film. The model is able to predict the differences in the observed discharge curves between LiTFSI/DMSO and the LiTFSI/TEGDME electrolytes based on prior assumptions, with a minimum of free parameters. The model parameters are all either based on physical characterization of the materials and the electrodes, or determined by fitting to impedance spectra recorded during the discharge. The ratio between the solution and surface mechanism was found to shift towards the latter with progressing discharge and hence increasing film thickness. The model and the methodology will provide a powerful tool for the optimization of electrodes for future Li–air batteries.

Declarations

References

1. Kraytsberg A, Ein-Eli Y (2011) J Power Sources 196(3):886
2. Mahne N, Fontaine O, Thotiyl MO, Wilkening M, Freunberger SA (2017) Chem Sci 8(10):6716
3. Ma L, Yu T, Tzoganakis E, Amine K, Wu T, Chen Z, Lu J (2018) Adv Energy Mater 8(22):1800348
4. Lu J, Li L, Park JB, Sun YK, Wu F, Amine K (2014) Chem Rev 114(11):5611
5. Johnson L, Li C, Liu Z, Chen Y, Freunberger SA, Ashok PC, Praveen BB, Dholakia K, Tarascon JM, Bruce PG (2014) Nat Chem 6(12):1091
6. Lyu Z, Zhou Y, Dai W, Cui X, Lai M, Wang L, Huo F, Huang W, Hu Z, Chen W (2017) Chem Soc Rev 46(19):6046
7. Augustin M, Vullum PE, Vullum-Bruer F, Svensson AM (2019) J Power Sources 414:130
8. Adams BD, Radtke C, Black R, Trudeau ML, Zaghib K, Nazar LF (2013) Energy Environ Sci 6(6):1772
9. Knudsen KB, Vegge T, McCloskey BD, Hjelm J (2016) J Electrochem Soc 163(9):A2065
10. Xue KH, McTurk E, Johnson L, Bruce PG, Franco AA (2015) J Electrochem Soc 162(4):A614
11. Laoire CO, Mukerjee S, Abraham K, Plichta EJ, Hendrickson MA (2009) J Phys Chem 113(46):20127
12. Laoire CO, Mukerjee S, Abraham K, Plichta EJ, Hendrickson MA (2010) J Phys Chem 114(19):9178
13. Fan W, Cui Z, Guo X (2013) J Phys Chem 117(6):2623
14. Mitchell RR, Gallant BM, Shao-Horn Y, Thompson CV (2013) J Phys Chem 4(7):1060
15. Xia C, Waletzko M, Chen L, Peppler K, Klar PJ, Janek J, Appl ACS (2014) Mater Interfaces 6(15):12083
16. Hardwick LJ, Bruce PG (2012) Curr Opin Solid ST M 16(4):178
17. Kumar V, Younes A, Nguyen K, Alía MOFJ, Jangwoo K, Giammona MJ, Ho-Cheol K, Young-Hye L (2019) Beilstein J Nanotechnol 10:930
18. Newman J, Tiedemann W (1975) Porous-electrode theory with battery applications. AIChE J 21(1):25–41
19. Li X, Huang J, Faghri A (2016) J Power Sources 332:420
20. Pan W, Yang X, Bao J, Wang M (2017) J Electrochem Soc 164(11):E3499
21. Torayev A, Magusin PC, Grey CP, Merlet C, Franco AA, Appl ACS (2018) Energy Mater 1(11):6433
22. Gwak G, Ju H (2016) Electrochim Acta 201:395
23. Wang D, Mu X, Ping H, Zhou H (2019) Mater Today 26:87
24. Ottakam Thotiyl MM, Freunberger SA, Peng Z, Yuhui C, Liu Z, Bruce PG (2013) Nat Mater 12(19):1050
25. Zhai D, Wang HH, Yang J, Lau KC, Li K, Amine K, Curtiss LA (2013) J Am Chem Soc 135:15364
26. Viswanathan V, Thygesen KS, Hummelshøj J, Nørskov JK, Girishkumar G, McCloskey B, Luntz A (2011) J Chem Phys 135(21):214704
27. Sahapatsombut U, Cheng H, Scott K (2013) J Power Sources 227:243
28. Horstmann B, Gallant B, Mitchell R, Bessler WG, Shao-Horn Y, Bazant MZ (2013) J Phys Chem 4(24):4217
29. Luntz AC, Viswanathan V, Voss J, Varley J, Nørskov J, Scheffler R, Speidel A (2013) J Phys Chem 4(20):3494
30. Xue KH, Nguyen TK, Franco AA (2014) J Electrochem Soc 161(8):E3028
31. Andrei P, Zheng JP, Hendrickson M, Plichta EJ (2012) J Electrochem Soc 159(6):A770
32. Albertus P, Girishkumar G, McCloskey B, Sánchez-Carrera RS, Kozinsky B, Christensen J, Luntz AC (2011) J Electrochem Soc 158(3):A343
33. Li X (2015) J Electrochem Soc 162(8):A1636
34. Bard AJ, Faulkner LR (2001) Electrochemical Methods: Fundamentals and Applications. Springer, New York
35. Speight JG et al (2005) Lange's handbook of chemistry. McGraw-Hill, New York
36. Liu B, Creager S (2010) J Power Sources 195(7):1812
37. Hirschorn B, Orazem ME, Tribollet B, Vivier V, Frateur I, Musiani M (2010) Electrochim Acta 55(21):6218
38. Huang J, Tong B (2017) ChemComm 53(83):11418
39. Højberg J, McCloskey BD, Hjelm J, Vegge T, Johansen K, Norby P, Luntz AC, Appl ACS (2015) Mater Interfaces 7(7):4039
40. Amin HM, Molls C, Bawol PP, Baltruschat H (2017) Electrochim Acta 245:967
41. Ottakam Thotiyl MM, Freunberger SA, Peng Z, Bruce PG (2012) J Am Chem Soc 135(1):494
42. Aetukuri NB, McCloskey BD, García JM, Krupp LE, Viswanathan V, Luntz AC (2015) Nat Chem 7(1):50
43. McCloskey BD, Scheffler R, Speidel A, Girishkumar G, Luntz AC (2012) J Phys Chem 116(45):23897
44. Lau S, Archer LA (2015) Nano Lett 15(9):5995
45. McCloskey BD, Speidel A, Scheffler R, Miller D, Viswanathan V, Hummelshøj J, Nørskov J, Luntz A (2012) J Phys Chem 3(8):997
46. Gualous H, Bouquain D, Berthon A, Kauffmann J (2003) J Power Sources 123(1):86
47. Kim DW, Ahn SM, Kang J, Suk J, Kim HK, Kang Y (2016) J Mater Chem 4(17):6332
48. Wong RA, Dutta A, Yang C, Yamanaka K, Ohta T, Nakao A, Waki K, Byon HR (2016) Chem Mater 28(21):8006

Authors and Affiliations

Michael T. Rauter[1,2] · **Matthias Augustin**[1] · **Lena Spitthoff**[1,3] · **Ann Mari Svensson**[1]

1. Department of Materials Science and Engineering, Norwegian University of Science and Technology, Trondheim, Norway

2. PoreLab, Department of Chemistry, Norwegian University of Science and Technology, Trondheim, Norway

3. Department of Energy and Process Engineering, Norwegian University of Science and Technology, Trondheim, Norway